Inorganic Chemistry

pubs.acs.org/IC
Article

Synthesis and Characterization of Ti^{4+} Containing Carbonates $Ti[CO_4]$ and $Ti_2O_3[CO_3]$

Lkhamsuren Bayarjargal,* Dominik Spahr, Victor Milman, Nico Giordano, Konstantin Glazyrin, and Björn Winkler

Cite This: *Inorg. Chem.* 2025, 64, 21893−21902
Read Online

ABSTRACT: Two titanium carbonates, $Ti[CO_4]$ and $Ti_2O_3[CO_3]$, were synthesized by the reaction of TiO_2 with CO_2 at high pressures and temperatures in a laser heated diamond anvil cell. Their structures were solved by in situ single crystal X-ray diffraction at high pressures. At pressures above ≈33 GPa, $Ti[CO_4]$-$I\bar{4}2d$ is stable. It transforms to $Ti[CO_4]$-$I4_1/amd$ on pressure release. The distinguishing feature of the $Ti[CO_4]$-structures is the presence of isolated $[CO_4]^{4-}$-groups, while $Ti_2O_3[CO_3]$ has isolated $[CO_3]^{2-}$-groups. Both structures contain 8-fold coordinated tetravalent Ti^{4+}-cations. Full geometry optimizations based on DFT calculations reproduced the crystal structures. The DFT models were used to complement the experimental compression data and for the assignment of Raman modes. While carbonates are typically compressible compounds, $Ti[CO_4]$ is rather incompressible with a bulk modulus of $K_0 \approx 200$ GPa. As we observed the pressure-induced transformation of TiO_2, we provide the Raman spectra of TiO_2−OI, and TiO_2−OII.

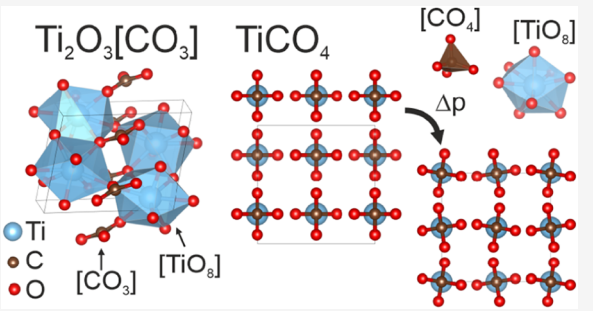

INTRODUCTION

In the last 15 years, our understanding of the crystal chemistry of carbonates has profoundly changed. In earlier reviews of carbonates, the common and characteristic feature of the ≈280 "conventional" carbonates was the presence of trigonal $[CO_3]^{2-}$-groups (e.g. refs 1 and 2). High pressure research led to a significant extension of the field of carbonate crystal chemistry and crystallography. Specifically, single crystal diffraction studies at high pressures unambiguously showed, that at very high pressures the carbon atom prefers a tetragonal coordination, forming $[CO_4]^{4-}$-groups, and is sp^3-hybridized[3] confirming the results of earlier powder diffraction based studies.[4] Several sp^3-carbonates have been obtained since.[5−16,16−19] In contrast to the conventional sp^2-carbonates, which have isolated $[CO_3]^{2-}$-groups, the $[CO_4]^{4-}$-groups can polymerize to form groups, rings, chains or pyramids. Their properties and stability fields are, however, still largely unexplored.

More recently, in situ high pressure studies of carbonates formed by reactions in laser heated diamond anvil cells have led to the discovery of pyrocarbonates, containing $[C_2O_5]^{2-}$-groups.[20,21] High pressure in situ single crystal studies have also shown that chemically simple carbonates, i.e., carbonates containing one type of metal cation only, with trivalent cations can be synthesized. Typical examples of the latter are carbonates containing trivalent cations such as $Al_2[CO_3]_3$, $Fe_2[CO_3]_3$, $Cr_2[CO_3]_3$, and $B[\mu\text{-}H(CO_3)_2]$ which contain Al^{3+}, Fe^{3+}, Cr^{3+}, and B^{3+} respectively.[22−25] More recently, we synthesized an iodide carbonate ($(IO_2)_2[CO_3]$) with a pentavalent iodide cation.[26]

The aim of the present study was to explore if a further extension of the crystal chemistry of carbonates is possible and if chemically simple anhydrous carbonates with tetravalent cations can be formed. Of course, a carbonate containing a Si^{4+} cation would be the most interesting phase, as it would be a potential storage material of carbon in the deep Earth. However, while some theoretical studies[27,28] predicted structures containing $[CO_3]^{2-}$-groups in the SiO_2−CO_2 system, none of these predictions have been confirmed by experiments.[29−32] Hence, we investigated the incorporation of Ti^{4+} instead. Ti^{4+} is the second most abundant tetravalent cation in the Earth's mantle after Si^{4+}, however, the abundance of titanium in the Earth is more than two orders smaller than that of silicon.[33] Also, there is a significant difference between the ionic radius of Si^{4+} and Ti^{4+} in octahedral coordination ($r(Si^{4+}) = 0.4$ Å $r(Ti^{4+}) = 0.6$ Å), the preferred coordination at ambient conditions differs (Si^{4+} is typically found in tetrahedral coordination, whereas Ti^{4+} prefers octahedral coordination)[34,35] and the electronic configuration is different. So

Received: July 2, 2025
Revised: October 14, 2025
Accepted: October 17, 2025
Published: October 27, 2025

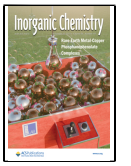

while a structural analogy between SiO_2 and TiO_2 was suggested at megabar pressures[36] structural correlations between Ti^{4+}- and Si^{4+}-bearing compounds may be limited at the moderate pressures investigated here.

CO_2 and TiO_2 have been found to coexist in inclusions of diamonds.[37] This finding offers the possibility of the presence of titanium carbonates in the mantle at high pressure and temperature conditions, where the diamonds were grown. There are very few complex natural carbonate minerals, such as sabinaite ($Na_4Zr_2TiO_4[CO_3]_4$), where tetravalent cations are incorporated by coupled substitution together with monovalent cations.[38] Structures for hypothetical anhydrous Ti-carbonates, such as $Ti[CO_3]_2$ and $Ti_2[CO_3]_3$ with space group symmetry $Pa\bar{3}$, have been predicted based on *ab initio* random structure searching technique.[39] However, these predictions have not been experimentally validated and neither a natural simple titanium carbonate has been found nor has such a phase been synthesized experimentally up to now.

In summary, it is currently unclear whether anhydrous chemically simple carbonates with tetravalent cations can form at high pressure and temperature conditions and what kind of structure they will have. The aim of the present study therefore addresses the formation and characterization of chemically simple anhydrous carbonates with tetravalent Ti^{4+} cations. We present the successful synthesis, characterization by Raman spectroscopy and X-ray diffraction of two new Ti-carbonates with the composition $Ti_2O_3[CO_3]$ and $Ti[CO_4]$ and discuss their unusual elastic properties.

METHODS

High-Pressure Experiments. We used a synthetic TiO_2 powder (99.5% purity, Alfa Aesar) and natural single rutile crystals (Großes Zirknitztal, Austria) for the high-pressure experiments. An additional characterization of the samples using SEM and energy dispersive X-ray spectroscopy (EDX) is provided in the Supporting Information (SI:EDX measurements of starting material and Figure S8).

The high-pressure experiments were carried out in diamond anvil cells (DACs) with Boehler-Almax design and 300 μm culet size.[40] We used rhenium as gasket material which was preindented to a thickness of ~45 μm. 120 μm gasket holes serving as sample chambers were drilled by a custom-built laser setup.

The compacted TiO_2 powder or natural single crystals of rutile with maximum dimensions of up to ~100 × 40 × 15 μm^3 and a ruby for pressure determination were placed in the gasket hole. Then, CO_2 was directly condensed into the sample chamber using a custom-built cryogenic loading system. In order to condense the CO_2 into the sample chamber, a slightly opened DAC was placed on a liquid nitrogen cooled Cu-holder to cool down the DAC to ~100 K. We used a small nozzle to direct a CO_2 gas jet directly on the diamonds and the gasket.[21] Ar was used as a purge-gas to avoid the precipitation of H_2O ice. The precipitation of the CO_2 in the gasket hole was monitored using an optical microscope. After a sufficient amount of CO_2 was gathered in the sample chamber, the DAC was tightly closed. CO_2 dry ice is less compressible than Ne or He, and hence the gasket hole does not shrink notably during compression.

The pressure was determined by measuring the shift of the ruby fluorescence assuming a potential error of 6% for deviations from hydrostatic conditions.[41] We estimate a pressure uncertainty of at least ~10% due to the pressure gradient and pressure change after laser heating. We additionally used the equation of states of the high pressure polymorphs of TiO_2, i.e., of cotunnite (orthorhombic II (TiO_2−OII)) and baddeleyite, as a pressure reference.[34,42,43] This allowed us to independently constrain the pressure conditions in the X-ray diffraction experiments.

Raman Spectroscopy and Laser Heating. High-pressure Raman spectroscopic measurements and the double-sided laser-heating were performed with a custom-built setup.[44] Raman spectroscopy was carried out with a Nd:YAG laser (λ = 532.14 nm, Cobolt-Samba, Hübner Photonics) in combination with a Princeton Instruments ACTON SpectraPro (SP-2356) spectrometer equipped with a Pixis 256E CCD camera. We used a Raman laser spot size on the sample of ~6 μm while using a laser power of 250 mW on the sample. Two-dimensional Raman maps were measured on a regular grid with a grid spacing of 6 μm. The Raman spectra were measured up to 2000 cm^{-1}, depending on the pressure. The background correction was performed using the software package Matlab.

We used a pulsed CO_2 laser (Coherent Diamond K-250) with λ = 10600 nm for double-sided laser-heating. The laser power was adjusted to 1−6 W to achieve coupling of the laser to the sample from both sides. Laser focusing on the sample results in a heating area of ~40 × 40 μm^2. The temperatures during the laser heating were determined by the two-color pyrometer method, employing Planck and Wien fits. Heating procedures in DACs may suffer from large temperature gradients, and the actual temperature is strongly dependent on the coupling of the laser with the sample. We estimate an uncertainty of at least ~10% of the nominal temperature in the laser heated region depending on specific laser heating conditions, based on typical 2D temperature-gradient determination experiments performed in DACs.[45]

Synchrotron Single Crystal Diffraction. Single crystal X-ray diffraction was performed at the PETRA III synchrotron (DESY) in Hamburg, Germany on the extreme conditions beamline P02.2.[46] The beam size on the sample was ≈2 × 2 μm^2 (fwhm), focused by Kirkpatrick-Baez mirrors. The diffraction data were collected using a PerkinElmer XRD1621 detector using either the wavelength of 0.2901 Å or 0.2904 Å. We collected multigrain single crystal data while rotating by ±33° around the axis perpendicular to the beam in the DAC while collecting frames in 0.5° steps with 4 s acquisition time per frame.

The detector to sample distances (412 mm and 425 mm) were calibrated with a CeO_2 standard using DIOPTAS.[47] At each experimental session, the instrument calibration was done using data collected from a single crystal of enstatite ($MgSiO_3$). After the measurement, the reflections were indexed and integrated employing CrysAlis^{PRO}. We used the Domain Auto Finder program (DAFi) to find possible single crystal domains for the subsequent data reduction.[48] The crystal structures in this study were solved using SHELXT.[49,50] After structure solution, the crystal structures were refined with SHELXL.[51] SHELXT and SHELXL programs were implemented in the Olex2 software package.[52] Some structure refinements were performed using the software package JANA2006.[53]

Density Functional Theory-Based Calculations. First-principles calculations were carried out within the framework of density functional theory (DFT), employing the Perdew−Burke−Ernzerhof (PBE) exchange-correlation functional and the plane wave/pseudopotential approach implemented in the CASTEP simulation package.[54−56] "On the fly" norm-conserving or ultrasoft pseudopotentials generated using the descriptors in the CASTEP database were employed in conjunction with plane waves up to a kinetic energy cutoff of 1020 or 630 eV, for norm-conserving and ultrasoft pseudopotentials, respectively. The accuracy of the pseudopotentials is well established.[57] A Monkhorst−Pack grid was used for Brillouin zone integrations.[58] We used a distance between grid points of <0.023 $Å^{-1}$. Convergence criteria for geometry optimization included an energy change of <5 × 10^{-6} eV $atom^{-1}$ between steps, a maximal force of <0.008 eV $Å^{-1}$ and a maximal component of the stress tensor <0.02 GPa.

Elastic stiffness coefficients were obtained by the strain−stress method. In the stress−strain method employed here, symmetry adapted-strain patterns were imposed on the fully optimized ground state structure. For each symmetry adapted strain atomic coordinates were relaxed, and the stress tensor was obtained for three to six different amplitudes. Elastic coefficients and their statistical errors were obtained from linear fitting of the stress−strain dependencies.[59]

https://doi.org/10.1021/acs.inorgchem.5c03033
Inorg. Chem. 2025, 64, 21893−21902

Phonon frequencies were obtained from density functional perturbation theory (DFPT) calculations.[60,61] Raman intensities were computed using DFPT with the "2n + 1" theorem approach.[62]

RESULTS AND DISCUSSION

Compression and Heating of TiO_2 + CO_2. Raman spectra of the mixture TiO_2 + CO_2 were obtained after laser heating up to 2600(300) K at 25, 35, and 40 GPa. During heating, CO_2−III transformed into CO_2−IV and partially into CO_2−V. These transitions can be conveniently followed by Raman spectroscopy. A sequence of high pressure polymorphs of TiO_2 are expected when rutile is used as precursor.[34,42,43] We obtained TiO_2−OI at around 20 GPa, which eventually transformed to TiO_2−OII at above 38 GPa. No carbonates were formed after heating at pressures 25 and 35 GPa, but a reaction occurred once we laser heated for a prolonged time at ∼40 GPa (Figure 1).

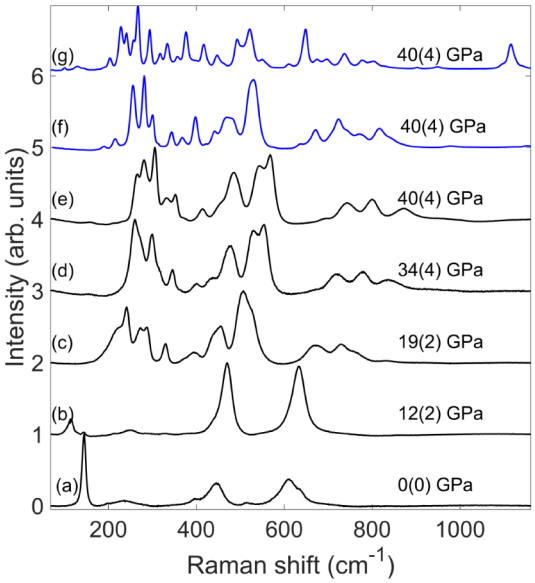

Figure 1. (a) Raman spectrum of starting sample TiO_2-rutile at ambient conditions. (b−d) Raman spectra of TiO_2 during compression without heating. (e) Raman spectra of samples before laser heating at 40(4) GPa. (f) Raman spectra of samples after short laser heating at 40(4) GPa, with conbtributions by TiO_2−OII and TiO_2−OI. (g) Raman spectra of samples after long laser heating at 40(4) GPa. The appearance of a Raman band close to 1200 cm^{-1} is indicative of the presence of a carbonate. There are Raman bands due to the new carbonate, TiO_2−OII and CO_2−V.

Structure of TiO_2−OII. From the single crystal X-ray diffraction experiment, we determined the structure of the high pressure polymorph of TiO_2−OII. It corresponds to the structure which was found in previous studies.[63,64] At 42 GPa, the lattice parameters of TiO_2−OII are a = 5.1097(7) Å, b = 2.9612(13) Å, c = 5.944(4) Å and V = 89.94(7)Å^3. (*Pnma*, Z = 4). The Ti atoms are 9-fold coordinated by oxygen with Ti−O-distances ranging from 1.932(4) to 2.259(4) Å with an average distance of 2.09(13) Å. The pressure-dependence of the unit-cell volume of TiO_2−OII phase is shown together with previous data of TiO_2−OII in Figure S1.[42] Tables S1 and S2 show our crystallographic data of TiO_2−OII, which has been deposited in the Cambridge Structural Database (CSD) under deposition numbers CCDC 2485339.

Structure of $Ti_2O_3[CO_3]$-*P2/c*. When heating TiO_2−OII, in three distinct experiments we observed new additional Raman peaks after laser heating above 40 GPa. This indicated the reaction of TiO_2 with the surrounding CO_2 and the formation of two new phases. The analysis of the synchrotron single crystal X-ray diffraction data of the first unknown phase showed that this was a titanium carbonate with the composition $Ti_2O_3[CO_3]$. After the data reduction the crystal structure was solved in the monoclinic space group $P2/c$ (No. 13) with Z = 2. The lattice parameters at 39(3) GPa are a = 6.4859(10) Å, b = 4.213(3) Å, c = 4.990(2) Å β = 101.71(2)° and V = 133.51(11) Å^3 (Tables S3−S6).

The structural parameters derived from experiments were employed as a trial structure in DFT calculations. The structure after the full geometry optimization was in good agreement with the experimental values, as the DFT calculations gave a = 6.4614 Å, b = 4.3257 Å, c = 5.0041 Å β = 101.785° and V = 136.92 Å^3 (Table S3).

This crystal structure contains isolated $[CO_3]^{2-}$-groups and Ti^{4+} cations. The Ti atoms are 8-fold coordinated by oxygen with Ti−O-distances ranging from 1.804(6) to 2.282(4) Å. The average Ti−O-distance is 2.02(16) Å. These interatomic distances are well in the range of typical Ti−O-distances in TiO_2−OII, which were determined by us at 42 GPa. The coordination polyhedra of the Ti-atoms form a network by sharing edges and corners. All carbon atoms are coordinated by three oxygen atoms forming a distorted triangle. The $[CO_3]^{2-}$-groups of $Ti_2O_3[CO_3]$ have one short (∼1.213(12) Å) and two longer (∼1.270(6) Å) C−O bonds. The shortest C−O bond is connected with the longest Ti−O bonds in the coordination polyhedra of Ti. Also, one O−C−O angle ϕ_1^{O-C-O}=115.3(7)° differs significantly from the other two angles with $\phi_{2,3}^{O-C-O}$=122.4(4)° in $[CO_3]$-groups. The coordination $[TiO_8]$-polyhedra and $[CO_3]$-groups are illustrated in Figure 2a. Each "double layers" of $[TiO_8]$-polyhedra are connected to each other with $[CO_3]$-groups (Figure 2a). The crystallographic data of $Ti_2O_3[CO_3]$-$P2/c$ has been deposited in the Cambridge Structural Database (CSD) under the deposition number CCDC 2416531.

Structure of $Ti[CO_4]$-$I\bar{4}2d$. The crystal structure solution and refinement of the second new phase showed that this is a novel inorganic titanium carbonate with $Ti[CO_4]$ composition. At 39(3) GPa, $Ti[CO_4]$ crystallizes in the tetragonal space group $I\bar{4}2d$ with Z = 4, a = 5.8124(9) Å, c = 5.080(3) Å and V = 171.62(11)Å^3. The structure of $Ti[CO_4]$-$I\bar{4}2d$ is shown in Figure 2b. This structure contains isolated $[CO_4]^{4-}$-carbonate groups and Ti^{4+}. The Ti^{4+} atom is 8-fold coordinated by oxygen with two different Ti−O-distances 1.9241(19) Å and 1.979(3) Å. The average bond Ti−O length is 1.9515 Å and is thus slightly shorter than Ti−O-distances in TiO_2−OII or $Ti_2O_3[CO_3]$. The $[TiO_8]$ polyhedra are irregularly shaped and form a network by sharing edges of polyhedra. Each$[CO_4]$-tetrahedra shares two edges with two different $[TiO_8]$-polyhedra.

The crystallographic parameters and details of the structure refinement of $Ti[CO_4]$-$I\bar{4}2d$ measured at 39(3) GPa are listed in Tables S7 and S8. The crystallographic data of $Ti[CO_4]$-$I\bar{4}2d$ has been deposited in the Cambridge Structural Database (CSD) under the deposition number CCDC 2416536.

The structural model derived from the experiments was employed as a trial structure for DFT full geometry

https://doi.org/10.1021/acs.inorgchem.5c03033
Inorg. Chem. 2025, 64, 21893−21902

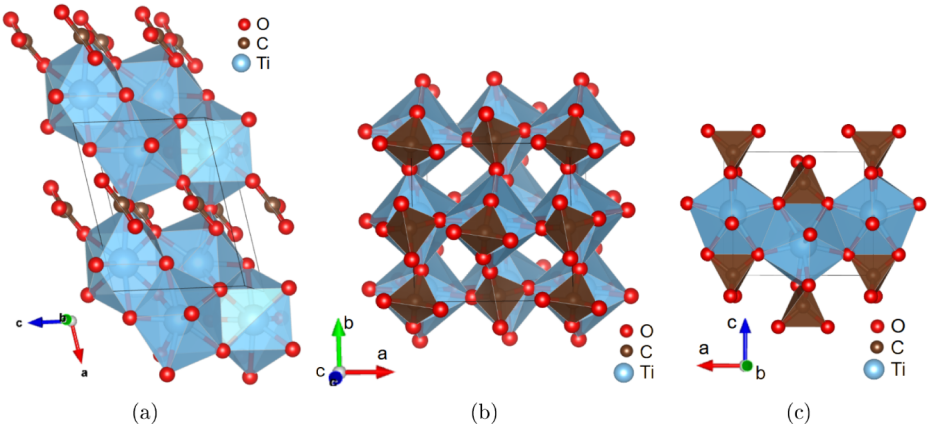

Figure 2. (a) The structure of $Ti_2O_3[CO_3]$ at 39(3) GPa, viewed along [010]. The structure contains isolated $[CO_3]$-groups and $[TiO_8]$-polyhedra. Each double layers of $[TiO_8]$-polyhedra are connected to each other with CO_3-groups. (b) The structure of $Ti[CO_4]$ at 39(3) GPa, viewed along [001]. The $[TiO_8]$-polyhedra and CO_3-groups are main building blocks of $Ti[CO_4]$. (c) The structure of $Ti[CO_4]$ at 39(3) GPa, viewed along [010].

optimizations. The two data sets are in the expected good agreement. A comparison can be found in Table S7.

Structure of $Ti[CO_4]$-$I4_1/amd$. On pressure release at lower pressures, $Ti[CO_4]$-$I\bar{4}2d$ undergoes a phase transition to a structure with the higher symmetry $I4_1/amd$. At 14.4(30) GPa, the crystal structure was solved and it was found that $Ti[CO_4]$ crystallizes in the tetragonal space group $I4_1/amd$ with $Z = 4$ (Figure 3).

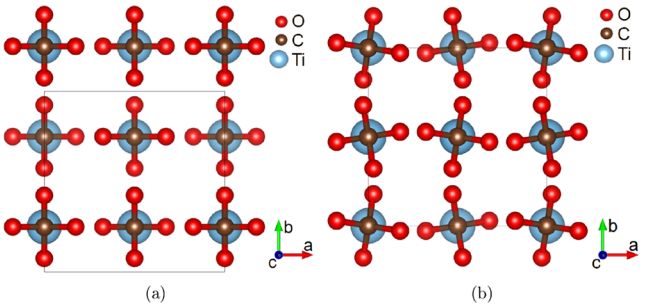

Figure 3. Structure viewed along [001] for (a) the low-pressure phase $Ti[CO_4]$-$I4_1/amd$ at 14.4(30) GPa and (b) the high pressure phase $Ti[CO_4]$-$I\bar{4}2dI\bar{4}2d$ at 39(3) GPa. The displacement of the oxygen atoms is responsible for the phase transition between both structures.

The structure solution results in unit cell parameters $a = b = 6.021(4)$ Å and $c = 5.185(2)$ Å for $Ti[CO_4]$-$I4_1/amd$. In $Ti[CO_4]$-$I4_1/amd$ there is one symmetrically independent Ti−O distance of 2.003(4) Å between Ti and O atoms, while in $Ti[CO_4]$-$I\bar{4}2d$ there are two symmetrically independent Ti−O-distances. All carbon atoms are tetrahedrally coordinated by oxygen atoms, where the interatomic Ti−O distances are 1.355(3) Å at 39(3) GPa and 1.374(3) Å at 14.4(30) GPa.

The $Ti[CO_4]$-$I4_1/amd$ structure is very similar to the structure of $Ti[CO_4]$-$I\bar{4}d$ at 39(3) GPa. The main difference is due to a displacement of the oxygen atoms from a special position in $I4_1/amd$ to the general position in $I\bar{4}2d$ with a concomitant rotation of the $[CO_4]$ tetrahedra around the c-axis. The displacement of the oxygen atoms is clearly discernible from a comparison of crystal structures at pressures of 39(3) GPa and of 14.4(30) GPa in Figure 3.

The crystallographic parameters and details of the structure refinement of $Ti[CO_4]$-$I4_1/amd$ measured at 14.4(30) GPa are listed in Tables S7 and S9. The crystallographic data of $Ti[CO_4]$-$I4_1/amd$ has been deposited in CSD under the deposition number CCDC 2416537. Here again, the structural parameters obtained from DFT full geometry optimizations are in good agreement with those determined experimentally.

Phase Transition of $Ti[CO_4]$. Our DFT calculations predict that the phase transition occurs around 31−35 GPa. In this pressure range, the volume of $Ti[CO_4]$-$I\bar{4}2d$ is ≈0.7% larger than that of $Ti[CO_4]$-$I4_1/amd$ (Figures 4 and S5). At

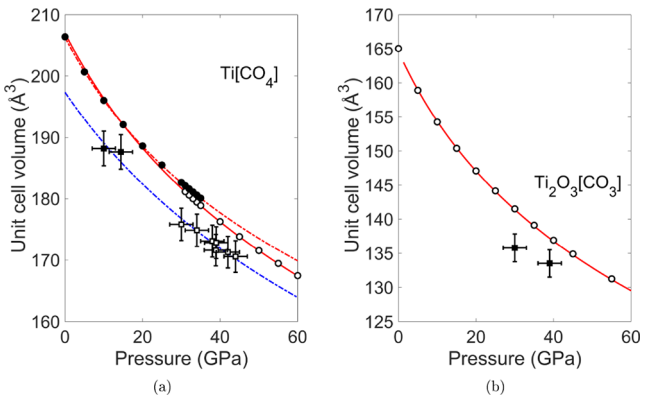

Figure 4. (a) Pressure-dependence of the unit-cell volumes of $Ti[CO_4]$. The dashed lines represents BM3-EOS which were fitted to the DFT data of $Ti[CO_4]$-$I4_1/amd$ (black circles) and $Ti[CO_4]$-$I\bar{4}2d$ (open cycles). The dashed blue line marks BM3-EOS fit of experimental data of $Ti[CO_4]$ (squares). (b) Pressure-dependence of the unit-cell volumes of $Ti_2O_3[CO_3]$. The DFT data (circles) were fitted using BM3-EOS (red line). Open squares show the experimental data.

≈30 GPa, X-ray diffraction data shows still $Ti[CO_4]$-$I\bar{4}2d$. Unfortunately, no X-ray data were collected between 30 and 14.4 GPa and therefore the accuracy of the predicted transition pressure cannot currently be assessed.

The crystal structures and chemical compositions of $Ti_2O_3[CO_3]$ and $Ti[CO_4]$ differ significantly from the previously predicted Ti-carbonate phases such as $Ti[CO_3]_2$ and $Ti_2[CO_3]_3$ with space group symmetry $Pa\bar{3}$.[39] Instead, $Ti[CO_4]$-$I4_1/amd$ is isostructural to zircon, $Zr[SiO_4]$. In $Zr[SiO_4]$ a phase transition from $I4_1/amd$ into $I\bar{4}2d$ was first

https://doi.org/10.1021/acs.inorgchem.5c03033
Inorg. Chem. 2025, 64, 21893−21902

predicted by calculations[65] and later confirmed by experiment.[66] This phase transition occurs 21.0(1) GPa and is driven by a Raman active soft-mode. In Ti[CO_4]-$I4_1/amd$, a A_u mode becomes soft at the Γ-point with increasing pressure, but this mode is not Raman active.

Bulk Modulus of $Ti_2O_3[CO_3]$ and Ti[CO_4]. The bulk modulus of both phases was obtained by fitting a third-order Birch−Murnaghan equation (BM3-EOS)[67,68] of states to volumes obtained by experiments and DFT-based calculations (Figure 4) using the EoSFit7 program.[69] The bulk moduli from BM3-EOS are given in Table 1 .

Table 1. Bulk Modulus Were Determined Using the Third-Order Birch-Murnaghan equation[67,68] of States (BM3-EOS) from Theoretical and Experimental Volumes of Unit Cells and Coordination Polyhedra and Using Stress-Strain Calculations (See Figure 4)

	Third-order BM-EOS		
0−60 GPa	K_0 (GPa)	V_0 (Å^3)	K_p
$Ti_2O_3[CO_3]$ (calc.)	131(2)	164(1)	5.4(1)
[TiO_8] in $Ti_2O_3[CO_3]$ (calc.)	139(3)	17.45(2)	5.5(1)
Ti[CO_4] (exp.)	212(25)	197(2)	4.5(1.8)
Ti[CO_4] (calc.)	192(9)	206(1)	3.9(3)
Ti[CO_4]-$I4_1$/amd (0−35 GPa, calc.)	166(1)	206.34(4)	6.5(1)
Ti[CO_4]-$I\bar{4}2d$ (31−65 GPa, calc.)	166(1)	207.00(4)	5.0(1)
[TiO_8] in Ti[CO_4] (calc.)	148(8)	16.07(4)	8.0(5)
[CO_4] in Ti[CO_4] (calc.)	397(24)	1.37(2)	8.9(1.2)
[CO_4] in Ti[CO_4] (0−35 GPa, calc.)	435(2)	1.3713(1)	4.1(1)
[CO_4] in Ti[CO_4] (31−65 GPa, calc.)	468(2)	1.3676(3)	5.9

The theoretical bulk modulus of $Ti_2O_3[CO_3]$ obtained from BM3-EOS is K_0 = 131(2) GPa for the calculated data between 0 and 60 GPa. This value is similar to highest bulk moduli (131 and 125 GPa) of carbonates with isolated [CO_3]-groups such as Ni[CO_3] or Co[CO_3] at ambient conditions.[70,71]

The complete elastic stiffness tensor was obtained for the ambient pressure structures of Ti[CO_4]-$I\bar{4}2d$ and Ti[CO_4]-$I4_1/amd$ from stress−strain calculations (Table S10). The bulk moduli computed from the elastic stiffness tensor are K_0(Ti[CO_4]-$I4_1/amd$) = 156(2) GPa and K_0(Ti[CO_4]-$I\bar{4}2d$) = 157(2) GPa.

Considering the bulk moduli obtained from BM3-EOS fits to theoretical data, both phases have same the bulk modulus K_0 = 166(1) GPa (Table 1), which is smaller than bulk moduli K_0 = 201(3) GPa of Ti[CO_4]-$I4_1/amd$ and K_0 = 204(1) GPa of Ti[CO_4]-$I\bar{4}2d$ from a fit with a BM2-EOS.

As expected, the bulk modulus of Ti[CO_4] is much higher than the bulk modulus of $Ti_2O_3[CO_3]$ or carbonates with isolated [CO_4]-groups (Ca_2CO_4: K_0 = 108(10) GPa.[16] It is smaller than the bulk modulus (K_0 = 227 GPa) of the isostructural silicate zircon.[72] Based on previously published bulk moduli of carbonates,[16,19−22,70,71,73,74] Ti[CO_4] is highly likely the most incompressible compound within the broad carbonate family.

Compression of $Ti_2O_3[CO_3]$ and Ti[CO_4]. To understand the origin of the relatively high bulk modulus of Ti[CO_4], we analyzed the compressibility of the coordination polyhedra and tilting angles in both structures. Figure 5 shows the DFT-calculated volumes of the CO_4 and [TiO_8] polyhedra together with fits using a BM3-EOS.

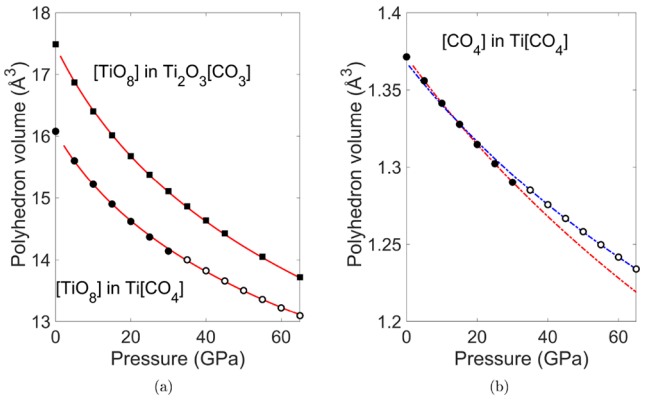

Figure 5. (a) Pressure-dependence of volumes of [TiO_8] polyhedra. The [TiO_8] polyhedron volumes of Ti[CO_4] are represented by open symbols and the corresponding polyhedron volumes of [TiO_8] in $Ti_2O_3[CO_3]$ by black symbols. The DFT data (circles) were fitted using and BM3-EOS (red lines). (b) Pressure-dependence of volumes of [CO_4]-polyhedra in Ti[CO_4]. The dashed blue line and open cycles represent BM3-EOS fit and DFT data of Ti[CO_4]-$I\bar{4}2d$. The dashed red line and black cycles represent BM3-EOS fit and DFT data of Ti[CO_4]-$I4_1/amd$.

The bulk modulus of the [TiO_8] polyhedra in $Ti_2O_3[CO_3]$ is 139(3) GPa. The compressibility of $Ti_2O_3[CO_3]$ is anisotropic (Figure 6a), where the *c*-axis is significantly less

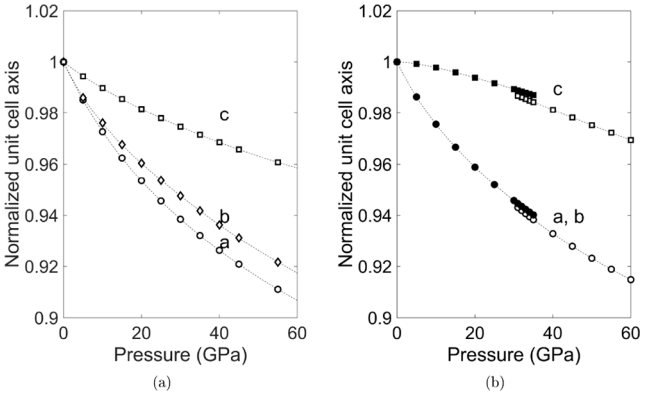

Figure 6. (a) Pressure dependence of the relative unit-cell parameters of $Ti_2O_3[CO_3]$ (b) Pressure dependence of the relative unit-cell parameters of Ti[CO_4] Filled symbols represent the Ti[CO_4]-$I4_1/amd$ phase, while open symbols refer to the Ti[CO_4]-$I\bar{4}2d$ phase. Dashed lines are guides to the eye.

compressible than the *a*- and *b*-axes. This can be rationalized by noting that the $[CO_3]^{2-}$-groups are essentially rigid and the [TiO_8] polyhedra are rather incompressible so that the major pressure induced structural changes are changes C−O−Ti angles. This is shown in Figure 7b,d, where the C−O−Ti angles ω_3 and ω_4 are strongly pressure-dependent, while the Ti−O−Ti angle ρ_2 increases only slightly. The effect of this is that the distance between the "double layers" shown in Figure 2a containing the [TiO_8]-polyhedra decreases on pressure increase, which makes the *a*-axis compressible. As there is a tilt between the [CO_3]-groups and the [TiO_8]-polyhedra, the *b*-axis is also compressible. The *c*-axis is rather incompressible, as a shortening of this axis would imply a decrease in Ti−Ti distances in the edge-sharing [TiO_8]-polyhedra, which is energetically unfavorable.

https://doi.org/10.1021/acs.inorgchem.5c03033
Inorg. Chem. 2025, 64, 21893−21902

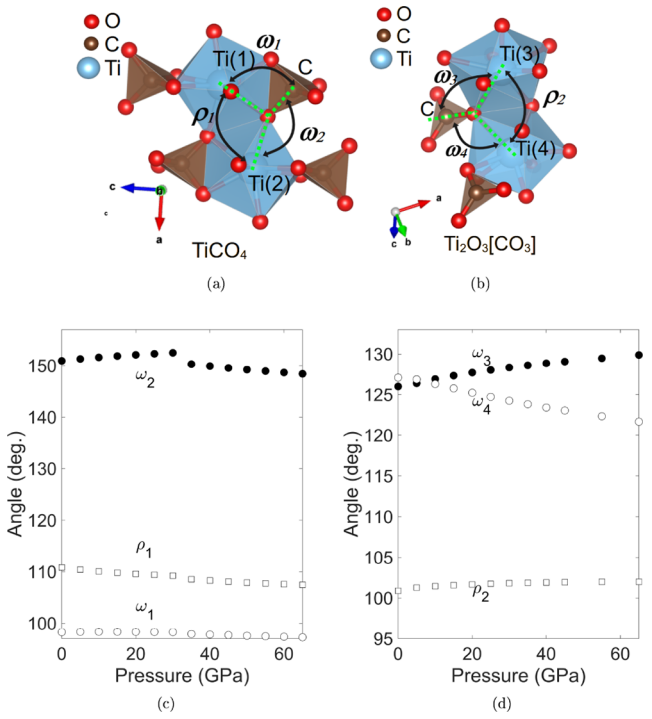

Figure 7. (a, b) Pressure-dependence of the angles between different atoms in Ti[CO_4] and $Ti_2O_3[CO_3]$. (c) Filled circles represent the ω_2 angle between C−O−Ti(2) in Ti[CO_4]. Open circles represent the ω_1 angle between C−O−T(1) and squares the ρ angle between Ti(1)−O−Ti(2) in Ti[CO_4]. (d) Filled circles represent the ω_3 angle between C−O−Ti(3) in $Ti_2O_3[CO_3]$. Open circles represent the ω_4 angle between C−O−Ti(4) and squares the angle between Ti(3)−O−Ti(4) in $Ti_2O_3[CO_3]$.

The bulk modulus of the TiO_8 polyhedra in Ti[CO_4] is 148(7) GPa, which is slightly higher than the value for the related polyhedra in $Ti_2O_3[CO_3]$. This is consistent with the slightly smaller volume of the [TiO_8] polyhedra in Ti[CO_4] (V_0(Ti[CO_4]) = 15.85(6) Å^3) compared to that in $Ti_2O_3[CO_3]$ (V_0($Ti_2O_3[CO_3]$) = 17.30(5) Å^3) (Figure 5a).

The [CO_4]-groups in Ti[CO_4] have a large bulk modulus, K_0 = 397 (24) GPa, due to the strong covalent bonding between the C- and O-atoms (Figure 5b and Table 1). Within the substantial error this value is similar to the bulk moduli of [CO_4]-groups in other carbonates such as Ca_2CO_4 (360(38) GPa).[16] It is slightly larger than the polyhedral bulk modulus of [SiO_4]-groups in most silicate garnets.[75]

The bulk modulus of Ti[CO_4] is in between the bulk moduli of the [TiO_8] polyhedra and [CO_4]-groups. The axial compression behavior of the *c*-axis is unusual in that it is slightly concave at low pressures for Ti[CO_4]-$I4_1/amd$. These two observations can be correlated again with the topology and the pressure-induced rotation of the constituent polyhedra. The angles are shown in Figure 7a, where ω_1 and ω_2 are C−O−Ti angles, while ρ_1 is a Ti−O−Ti angle. As is shown in Figure 7c, ω_2 increases during the compression of the Ti[CO_4]-$I4_1/amd$-phase, then discontinuously jumps to a lower value at the phase transition, and decreases on further compression. All other angles remain essentially unchanged. The consequence of this change is that essentially rigid units comprising a [TiO_8] and two [CO_4]-groups (Figure 7a) move with respect to one another, leading to compressible *a*- and *b*-axes and the concave behavior of *c*-axes in Ti[CO_4].

Raman Spectroscopy. Spatially resolved Raman measurements allowed us to locate the individual phases in the DAC after laser heating. This is shown in Figure 8.

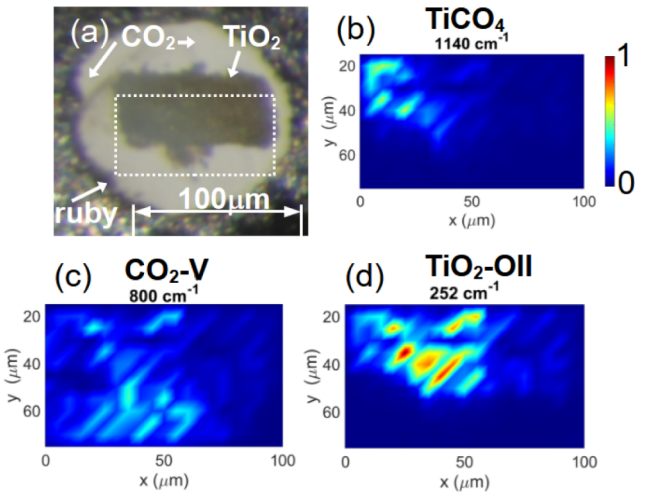

Figure 8. (a) Optical microscopic image of compacted TiO_2 powder and CO_2 in the DAC before laser heating at 40(4) GPa. The area in which spatially resolved Raman spectra were collected is indicated by a dashed square. After laser heating and temperature quenching, three phases could be identified at 40 GPa. (b) A Raman map of the 1140 cm^{-1} band shows the location of Ti[CO_4], (c) the distribution of CO_2−V was mapped by the band at 800 cm^{-1} (d) TiO_2−OII was located by mapping a Raman band at 252 cm^{-1}.

DFPT-calculations of the Raman spectra complemented the measurements and provided a link between structural and spectroscopic properties. The Raman map allowed us to select regions in which mainly a single phase, either TiO_2−OI, TiO_2−OII, CO_2−V or Ti[CO_4]-$I\bar{4}2d$ could be measured. In Figure 9 experimental and DFPT-Raman spectra obtained at different locations in the DAC are compared to each other.

As can be seen from Figure 9a, the most intense Raman band of TiO_2−OI can be found at ∼277 cm^{-1} at pressure of 38(4) GPa. Three further intense bands are located at ∼298, 391, and 511 cm^{-1}. To the best of our knowledge, this is the first time a Raman spectrum of TiO_2−OI has been obtained. The DFPT model calculations reproduce the spectrum very well, thus allowing an assignment of bands to eigenvectors.

Similarly, at 38(4) GPa, the most intense Raman band of TiO_2−OII is located at ∼252 cm^{-1} and another prominent Raman band is at ∼526 cm^{-1} (Figure 9b). More than 11 other modes of TiO_2−OII were observed in a range of 250−807 cm^{-1}. This is also the first time a Raman spectrum of TiO_2−OII has been published. Here again, the DFPT calculations reproduce the experimental spectrum well and can be employed to understand the corresponding displacement vectors.

After the reaction was induced by laser heating, characteristic Raman modes of Ti[CO_4] can be observed unequivocally at ∼648 and ∼1125 cm^{-1}, in addition to the Raman modes of TiO_2 and CO_2−V Figure 9). The irreducible representations of Ti[CO_4]-$I\bar{4}2d$ at the Γ-point result in $\Gamma_{tot} = 3A_1 + 3A_2 + 5B_1 + 5B_2 + 10E$. The acoustic phonons are $\Gamma_{acoustic} = B_2 + E$. The Raman active modes are $\Gamma_{Raman} = 3A_1 + 5A_2 + 4B_1 + 9E$ while the $\Gamma_{IR} = 4B_2 + 9E$ modes are infrared active. We have clearly identified 11 of the 21 Raman active modes at ambient conditions in the range between 60 cm^{-1} and 1200 cm^{-1} at

https://doi.org/10.1021/acs.inorgchem.5c03033
Inorg. Chem. 2025, 64, 21893−21902

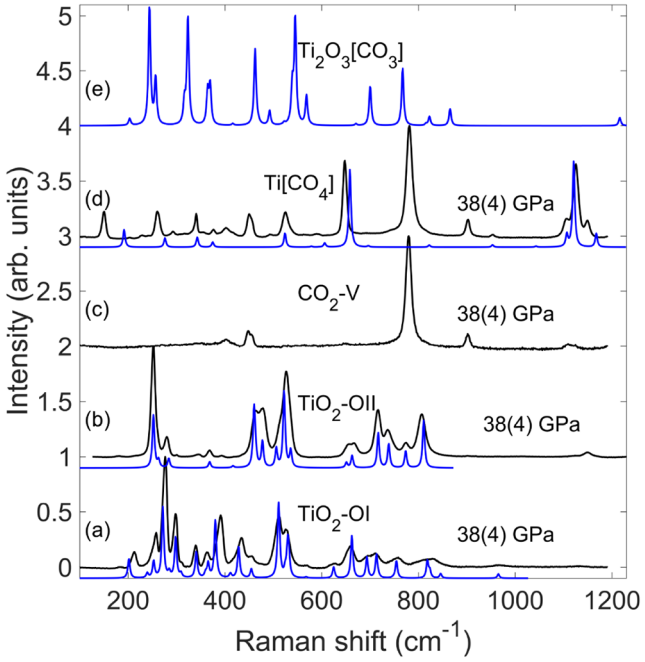

Figure 9. Raman spectra of TiO_2−OI (a), TiO_2−OII (b), CO_2−V (c), Ti[CO_4]-$I\bar{4}2d$ (d) and $Ti_2O_3[CO_3]$ (e). Experimental Raman spectra (black line) were collected at 38(4) GPa after laser heating quenched to ambient temperature. Theoretical (blue line) Raman spectra frequencies were calculated at 40 GPa and scaled by 4.1% to account for the well-established GGA-PBE underbinding.

38(4) GPa. Using the DFPT calculations, which reproduce the Raman spectrum very well, we found that the characteristic band at 1125^{-1} with very strong intensity can be attributed to the vibration of Ti-Atoms along the *c*-axis (Figure 9d). The second intense Raman band of Ti[CO_4] is separated from other bands at ∼648 cm^{-1}, and reflects the vibration of oxygen atoms in the[CO_4]-groups. Lattice modes with similarly intense peaks have energies of 525, 341, 260, and 151 cm^{-1}.

In $Ti_2O_3[CO_3]$−*P*2/*c*, each unit cell contains two formula units and hence there are 54 normal modes (Γ_{tot} = 12A_g + 12A_u + 15B_g + 15B_u). After subtraction of the 3 acoustic phonons ($\Gamma_{acoustic}$ = A_u + 2B_u), the irreducible representations of the optical vibrations of $Ti_2O_3[CO_3]$ at the Γ-point is Γ_{optic} = 12A_g + 11A_u + 15B_g + 15B_u where Γ_{Raman} = 12A_g + 15B_g are Raman active while the infrared active modes have representations Γ_{IR} = 11A_u + 13B_u. Our calculated Raman spectrum of $Ti_2O_3[CO_3]$ shows five strong characteristic Raman modes between 240−550 cm^{-1} and a very weak symmetric stretching mode of [CO_3]-groups around 1216 cm^{-1} (Figure 9). Unfortunately, these strong peaks overlapped with the Raman peaks of the major phases such as Ti[CO_4] and TiO_2 in our experiments. Because $Ti_2O_3[CO_3]$ was present in small quantities as a minor phase only, it was impossible to collect a clear Raman spectrum of this phase.

Stability. We have shown that $Ti_2O_3[CO_3]$ and Ti[CO_4] can be formed by the reactions (TiO_2 + CO_2 = Ti[CO_4] and 2TiO_2 + CO_2 = $Ti_2O_3[CO_3]$) of TiO_2 with CO_2. In most experiments we used synthetic TiO_2 samples as starting material. In the case of natural samples, we obtained the same results. While a more detailed analysis of the reaction would be desirable, it should be noted that the reactions take place with molten CO_2. There is currently no *p*, *V*, *T*-data available for CO_2 at the conditions employed here, and hence properties such as reaction volumes at high pressures and high temperatures cannot be reliably obtained.

Currently we can only present a few constraints based on our experiments regarding the stability field of both Ti-carbonates. During brief heating at pressures ranging from 25 to 35 GPa, Ti-carbonates were not readily formed. This might be the result of too low temperatures or these conditions are just outside the stability field of carbonate formation. Therefore, the determination of the stability field of Ti[CO_4] and $Ti_2O_3[CO_3]$ requires further theoretical and experimental studies.

CONCLUSIONS

We provided a detailed study of the synthesis, crystal structures, Raman data and elastic properties of two new Ti-carbonates, $Ti_2O_3[CO_3]$ and Ti[CO_4]. Both structures contain Ti^{4+}-cations and are the first two examples of anhydrous, chemically simple carbonates incorporating a tetravalent transition metal cation. We have solved both crystal structures and established their characteristic Raman signatures.

While $Ti_2O_3[CO_3]$ contains isolated trigonal $[CO_3]^{2-}$, the Ti[CO_4]-structure is characterized by the presence of isolated $[CO_4]^{4-}$-carbonate groups. Both structures contain 8-fold coordinated tetravalent Ti^{4+}-cations. The bulk modulus of Ti[CO_4] is around K_0 ≈ 200 GPa, while $Ti_2O_3[CO_3]$ has a bulk modulus in the range of K_0 ≈ 131−162 GPa. However, further experimental studies with X-diffraction are required to determine the bulk modulus more precisely. The compact packing of edge-sharing and incompressible [TiO_8] polyhedra with CO_4-groups explains the large incompressibility of Ti[CO_4] compared to other carbonates. The tilting of [TiO_8]-polyhedra against [CO_4]- or [CO_3]-groups governs the compression behavior, and explains the anisotropic compressibilities of the unit cells of Ti[CO_4] and $Ti_2O_3[CO_3]$.

Ti[CO_4]-*I*41/*amd* is isostructural to zircon, Zr[SiO_4], and the pressure-induced phase transition seems to be similar to the phase transition in Zr[SiO_4] transforming from $I4_1/amd$to $I\bar{4}2d$ under compression. It would be desirable to better understand the volume change at the transition. However, as the predicted volume change is smaller than 1%, it will be challenging to detect the transition using X-diffraction, similar to what has been the case for Zr[SiO_4].[65,66]

Since the amount of carbon in the mantle and the incorporation of carbon in mantle minerals is still being discussed controversially[76] the synthesis and characterization of anhydrous Ti-bearing carbonates constitutes a significant extension of the established crystal chemistry of carbonates with the potential to have a significant impact on our understanding of the deep carbon cycle. The simultaneous existence of CO_2 and TiO_2 in inclusions of diamonds offers direct evidence for the presence of TiO_2 and CO_2 in the mantle at conditions where the diamonds are forming.[37] Hence, once the stability fields of the Ti-carbonates obtained here are better constrained, their role as carbon hosts in the deep carbon cycle should be reassessed.

ASSOCIATED CONTENT

Supporting Information

The Supporting Information is available free of charge at https://pubs.acs.org/doi/10.1021/acs.inorgchem.5c03033.

https://doi.org/10.1021/acs.inorgchem.5c03033
Inorg. Chem. 2025, 64, 21893−21902

Additional experimental details, the results of the single crystal structure solution, and DFT-based calculations, including cif-files (PDF)

Accession Codes

Deposition numbers 2416531, 2416536−2416537, and 2485339 contain the supplementary crystallographic data for this paper. These data can be obtained free of charge via the joint Cambridge Crystallographic Data Centre (CCDC) and Fachinformationszentrum Karlsruhe Access Structures service.

AUTHOR INFORMATION

Corresponding Author

Lkhamsuren Bayarjargal − *Institute of Geosciences, Goethe University Frankfurt, Frankfurt 60438, Germany;* orcid.org/0000-0002-5513-591X; Email: bayarjargal@kristall.uni-frankfurt.de

Authors

Dominik Spahr − *Institute of Geosciences, Goethe University Frankfurt, Frankfurt 60438, Germany;* orcid.org/0000-0003-0489-5270

Victor Milman − *Dassault Systémes BIOVIA, Cambridge Cb4 0wn, United Kingdom;* orcid.org/0000-0003-2258-1347

Nico Giordano − *Deutsches Elektronen-Synchrotron DESY, Hamburg 22607, Germany;* orcid.org/0000-0001-9518-1251

Konstantin Glazyrin − *Deutsches Elektronen-Synchrotron DESY, Hamburg 22607, Germany*

Björn Winkler − *Institute of Geosciences, Goethe University Frankfurt, Frankfurt 60438, Germany;* orcid.org/0000-0001-8029-478X

Complete contact information is available at: https://pubs.acs.org/10.1021/acs.inorgchem.5c03033

Notes

The authors declare no competing financial interest.

ACKNOWLEDGMENTS

We gratefully acknowledge funding from the DFG (projects BA4020, BY101/2-1, and WI1232) and the DFG-Research Unit FOR2125/CarboPaT. BW is grateful for support by the Dassault Systemes Science Ambassador program. We acknowledge DESY (Hamburg, Germany), a member of the Helmholtz Association HGF, for the provision of experimental facilities. Parts of this research were carried out at PETRA III, beamline P02.2.

REFERENCES

(1) Railsback, L. B. Patterns in the compositions, properties, and geochemistry of carbonate minerals. *Carbonates Evaporites* **1999**, *14*, 1−20.

(2) *Carbonates: mineralogy and Chemistry*, Reeder, R. J., ed.; Walter de Gruyter GmbH & Co KG: Berlin, Boston, 1983.

(3) Merlini, M.; Hanfland, M.; Salamat, A.; Petitgirard, S.; Müller, H. The crystal structures of $Mg_2Fe_2C_4O_{13}$, with tetrahedrally coordinated carbon, and Fe_{13} O_{19}, synthesized at deep mantle conditions. *Am. Mineral.* **2015**, *100*, 2001−2004.

(4) Boulard, E.; Gloter, A.; Corgne, A.; Antonangeli, D.; Auzende, A.-L.; Perrillat, J.-P.; Guyot, F.; Fiquet, G. New host for carbon in the deep Earth. *Proc. Natl. Acad. Sci. U.S.A.* **2011**, *108*, 5184−5187.

(5) Cerantola, V.; Bykova, E.; Kupenko, I.; Merlini, M.; Ismailova, L.; McCammon, C.; Bykov, M.; Chumakov, A. I.; Petitgirard, S.; Kantor, I.; et al. Stability of iron-bearing carbonates in the deep Earth's interior. *Nat. Commun.* **2017**, *8*, 15960.

(6) Binck, J.; Bayarjargal, L.; Lobanov, S. S.; Morgenroth, W.; Luchitskaia, R.; Pickard, C. J.; Milman, V.; Refson, K.; Jochym, D. B.; Byrne, P.; Winkler, B. Phase stabilities of $MgCO_3$ and $MgCO_3$-II studied by Raman spectroscopy, X-ray diffraction, and density functional theory calculations. *Phys. Rev. Mater.* **2020**, *4*, 055001−1.

(7) Chariton, S. *The elastic properties and the crystal chemistry of carbonates in the deep Earth*, Ph.D. thesis; University of Bayreuth, 2019.

(8) Boulard, E.; Pan, D.; Galli, G.; Liu, Z.; Mao, W. L. Tetrahedrally coordinated carbonates in Earth's lower mantle. *Nat. Commun.* **2015**, *6*, 6311−1.

(9) Merlini, M.; Cerantola, V.; Gatta, G. D.; Gemmi, M.; Hanfland, M.; Kupenko, I.; Lotti, P.; Müller, H.; Zhang, L. Dolomite-IV: Candidate structure for a carbonate in the Earth's lower mantle. *Am. Mineral.* **2017**, *102*, 1763−1766.

(10) Oganov, A. R.; Ono, S.; Ma, Y.; Glass, C. W.; Garcia, A. Novel high-pressure structures of $MgCO_3$, $CaCO_3$ and CO_2 and their role in Earth's lower mantle. *Earth Planet. Sci. Lett.* **2008**, *273*, 38−47.

(11) Maeda, F.; Ohtani, E.; Kamada, S.; Sakamaki, T.; Hirao, N.; Ohishi, Y. Diamond formation in the deep lower mantle: a high-pressure reaction of $MgCO_3$ and SiO_2. *Sci. Rep.* **2017**, *7* (1), 40602.

(12) Oganov, A. R.; Glass, C. W.; Ono, S. High-pressure phases of $CaCO_3$: Crystal structure prediction and experiment. *Earth Planet. Sci. Lett.* **2006**, *241*, 95−103.

(13) Ono, S.; Kikegawa, T.; Ohishi, Y. High-pressure transition of $CaCO_3$. *Am. Mineral.* **2007**, *92*, 1246−1249.

(14) Pickard, C. J.; Needs, R. J. Structures and stability of calcium and magnesium carbonates at mantle pressures. *Phys. Rev. B* **2015**, *91*, 104101−1.

(15) Lobanov, S. S.; Dong, X.; Martirosyan, N. S.; Samtsevich, A. I.; Stevanovic, V.; Gavryushkin, P. N.; Litasov, K. D.; Greenberg, E.; Prakapenka, V. B.; Oganov, A. R.; Goncharov, A. F. Raman spectroscopy and X-ray diffraction of sp^3-$CaCO_3$ at lower mantle pressures. *Phys. Rev. B* **2017**, *96*, 104101−1.

(16) Binck, J.; Laniel, D.; Bayarjargal, L.; Khandarkhaeva, S.; Fedotenko, T.; Aslandukov, A.; Glazyrin, K.; Milman, V.; Chariton, S.; Prakapenka, V. B.; Dubrovinskaia, N.; Dubrovinsky, L.; Winkler, B. Synthesis of calcium orthocarbonate, Ca_2CO_4-*Pnma* at conditions of Earth's transition zone and lowermantle. *Am. Mineral.* **2022**, *107*, 336−342.

(17) Laniel, D.; Binck, J.; Winkler, B.; Vogel, S.; Fedotenko, T.; Chariton, S.; Prakapenka, V.; Milman, V.; Schnick, W.; Dubrovinsky, L.; Dubrovinskaia, N. Synthesis, crystal structure and structure-property relations of strontium orthocarbonate, Sr_2CO_4. *Acta Crystallogr.* **2021**, *B77*, 131−137.

(18) Spahr, D.; König, J.; Bayarjargal, L.; Luchitskaia, R.; Morgenroth, W.; Comboni, D.; Milman, V.; Winkler, B. Tetrahedrally Coordinated sp^3-Hybridized Carbon in Sr_2CO_4 Orthocarbonate at Ambient Conditions. *Inorg. Chem.* **2021**, *60*, 5419−5422.

(19) Spahr, D.; König, J.; Bayarjargal, L.; Gavryushkin, P. N.; Liermann, H.-P.; Milman, V.; Winkler, B. $Sr_3[CO_4]O$-antiperovskite with tetrahedrally-coordinated sp^3-hybridized carbon and OSr_6-octahedra. *Inorg. Chem.* **2021**, *60*, 14504−14508.

(20) Spahr, D.; König, J.; Bayarjargal, L.; Milman, V.; Perlov, A.; Liermann, H.-P.; Winkler, B. $Sr[C_2O_5]$ is an Inorganic Pyrocarbonate Salt with $C_2O_5]^{2-}$ Complex Anions. *J. Am. Chem. Soc.* **2022**, *144*, 2899−2904.

(21) Spahr, D.; König, J.; Bayarjargal, L.; Luchitskaia, R.; Milman, V.; Perlov, A.; Liermann, H.-P.; Winkler, B. Synthesis and Structure of $Pb[C_2O_5]$: An Inorganic Pyrocarbonate Salt. *Inorg. Chem.* **2022**, *61*, 9855−9859.

(22) Bayarjargal, L.; Spahr, D.; Milman, V.; Marquardt, J.; Giordano, N.; Winkler, B. Anhydrous Aluminum Carbonates and Isostructural Compounds. *Inorg. Chem.* **2023**, *62*, 13910−13918.

(23) Bayarjargal, L.; Spahr, D.; Bykova, E.; Wang, Y.; Giordano, N.; Milman, V.; Winkler, B. High-Pressure Synthesis of an Iron Carbonate, $Fe_2[CO_3]_3$. *Inorg. Chem.* **2024**, *63*, 21637−21644.

(24) Wang, Y.; Bayarjargal, L.; Bykov, M.; Bykova, E.; Spahr, D.; Glazyrin, K.; Milman, V.; Winkler, B. Cr^{3+}-Containing Carbonates and Cr_2O_3-Pbcn at Extreme Conditions. *Inorg. Chem.* **2025**, *64*, 4996−5003.
(25) Spahr, D.; Reuter, T. H.; Bykova, E.; Bayarjargal, L.; Bruening, L.; Kovalev, V.; Bykov, M.; Wedek, L.; Milman, V.; Wright, J.; Winkler, B.; et al. $B[\mu-H(CO_3)_2]$: An Acentric Boron Hydrogencarbonate with $[\mu-H(CO_3)_2]^{3-}$-Complex Anions. *Inorg. Chem.* **2025**, *64* (38), 19146−19150.
(26) Spahr, D.; Bayarjargal, L.; Brüening, L.; Kovalev, V.; Bykova, E.; Bykov, M.; Milman, V.; Mezouar, M.; Winkler, B.Synthesis and Crystal Structure of Anhydrous Di-iodyl Carbonate $I_2[CO_3]O_4$, Hosting I^{5+}-Cations. *JACS Au*, **2025**. .
(27) Yong, X.; Tse, J. S.; Chen, J. Mechanism of Chemical Reactions between SiO_2 and CO_2 under Mantle Conditions. *ACS Earth Space Chem.* **2018**, *2*, 548−555.
(28) Marques, M.; Morales-Garcia, A.; Menendez, J. M.; Baonza, V. G.; Recio, J. M. A novel crystalline SiCO compound. *Phys. Chem. Chem. Phys.* **2015**, *17*, 25055−25060.
(29) Santamaría-Pérez, D.; Marqueño, T.; MacLeod, S.; Ruiz-Fuertes, J.; Daisenberger, D.; Chulia-Jordan, R.; Errandonea, D.; Jordá, J. L.; Rey, F.; McGuire, C.; et al. Structural evolution of CO_2-filled pure silica LTA zeolite under high-pressure high-temperature conditions. *Chem. Mater.* **2017**, *29* (10), 4502−4510.
(30) Marqueno, T.; Santamaria-Perez, D.; Ruiz-Fuertes, J.; Chulia-Jordan, R.; Jorda, J. L.; Rey, F.; McGuire, C.; Kavner, A.; MacLeod, S.; Daisenberger, D.; et al. An ultrahigh CO_2-loaded silicalite-1 zeolite: Structural stability and physical properties at high pressures and temperatures. *Inorg. Chem.* **2018**, *57*, 6447−6455.
(31) Santoro, M.; Gorelli, F. A.; Bini, R.; Salamat, A.; Garbarino, G.; Levelut, C.; Cambon, O.; Haines, J. Carbon enters silica forming a cristobalite-type CO_2−SiO_2 solid solution. *Nat. Commun.* **2014**, *5* (1), 3761.
(32) Santamaría-Perez, D.; McGuire, C.; Makhluf, A.; Kavner, A.; Chuliá-Jordan, R.; Jorda, J. L.; Rey, F.; Pellicer-Porres, J.; Martinez-García, D.; Rodriguez-Hernández, P.; et al. Correspondence: Strongly-driven Re+ CO_2 redox reaction at high-pressure and high-temperature. *Nat. Commun.* **2016**, *7* (1), 13647.
(33) McDonough, W. F.; Sun, S.-S. The composition of the Earth. *Chem. Geol.* **1995**, *120*, 223−253.
(34) Gerward, L.; Staun Olsen, J. Post-rutile high-pressure phases in TiO_2. *J. Appl. Crystallogr.* **1997**, *30*, 259−264.
(35) Hemley, R. J.; Cohen, R. E. Silicate perovskite. *Annu. Rev. Earth Planet. Sci.* **1992**, *20*, 553−600.
(36) Duwal, S.; McCoy, C. A.; Weck, P. F.; Kalita, P.; Hanshaw, H. L.; Cochrane, K.; Ao, T.; Root, S. High-precision equation of state data for TiO_2: A structural analog of SiO_2. *Phys. Rev. B* **2020**, *102*, 024105.
(37) Smith, E. M.; Kopylova, M. G.; Frezzotti, M. L.; Afanasiev, V. P. Fluid inclusions in Ebelyakh diamonds: Evidence of CO_2 liberation in eclogite and the effect of H_2O on diamond habit. *Lithos* **2015**, *216*−*217*, 106−117.
(38) McDonald, A. M. The crystal structure of sabinaite, $Na_4Zr_2TiO_4(CO_3)_4$. *Can. Mineral.* **1996**, *34*, 811−815.
(39) Nelson, J. R.; Needs, R. J.; Pickard, C. J. Navigating the Ti-C-O and Al-C-O ternary systems through theory-driven discovery. *Phys. Rev. Mater.* **2021**, *5*, 123801.
(40) Boehler, R. New diamond cell for single−crystal X-ray diffraction. *Rev. Sci. Instrum.* **2006**, *77* (11), 115103.
(41) Mao, H. K.; Xu, J.; Bell, P. M. Calibration of the ruby pressure gauge to 800 kbar under quasi-hydrostatic conditions. *J. Geophys. Res.* **1986**, *91*, 4673−4676.
(42) Nishio-Hamane, D.; Shimizu, A.; Nakahira, R.; Niwa, K.; Sano-Furukawa, A.; Okada, T.; Yagi, T.; Kikegawa, T. The stability and equation of state for the cotunnite phase of TiO_2 up to 70 GPa. *Phys. Chem. Miner.* **2010**, *37*, 129−136.
(43) Al-Khatatbeh, Y.; Lee, K. K. M.; Kiefer, B. High-pressure behavior of TiO_2 as determined by experiment and theory. *Phys. Rev. B* **2009**, *79*, 134114.
(44) Bayarjargal, L.; Fruhner, C.-J.; Schrodt, N.; Winkler, B. $CaCO_3$ phase diagram studied with Raman spectroscopy at pressures up to 50 GPa and high temperatures and DFT modeling. *Phys. Earth Planet. Inter.* **2018**, *281*, 31−45.
(45) Du, Z.; Amulele, G.; Benedetti, L. R.; Lee, K. K. M. Mapping temperatures and temperature gradients during flash heating in a diamond-anvil cell. *Rev. Sci. Instrum.* **2013**, *84* (7), 075111.
(46) Liermann, H.-P.; Konôpková, Z.; Morgenroth, W.; Glazyrin, K.; Bednarčik, J.; McBride, E. E.; Petitgirard, S.; Delitz, J. T.; Wendt, M.; Bican, Y.; Ehnes, A.; Schwark, I.; Rothkirch, A.; Tischer, M.; Heuer, J.; Schulte-Schrepping, H.; Kracht, T.; Franz, H. The Extreme Conditions Beamline P02.2 and the Extreme Conditions Science Infrastructure at PETRA III. *J. Synchrotron Radiat.* **2015**, *22*, 908−924.
(47) Prescher, C.; Prakapenka, V. B. *DIOPTAS*: a program for reduction of two-dimensional X-ray diffraction data and data exploration. *High. Press. Res.* **2015**, *35*, 223−230.
(48) Aslandukov, A.; Aslandukov, M.; Dubrovinskaia, N.; Dubrovinsky, L. Domain Auto Finder (DAFi) program: the analysis of single-crystal X-ray diffraction data from polycrystalline samples. *J. Appl. Crystallogr.* **2022**, *55*, 1383−1391.
(49) Sheldrick, G. M. SHELXT − Integrated space-group and crystal-structure determination. *Acta Crystallogr.* **2015**, *71*, 3−8.
(50) Sheldrick, G. M. A short history of SHELX. *Acta Cryst. A* **2008**, *64*, 112−122.
(51) Sheldrick, G. M. Crystal structure refinement with SHELXL. *Cryst. Struct. Commun.* **2015**, *71*, 3−8.
(52) Dolomanov, O. V.; Bourhis, L. J.; Gildea, R. J.; Howard, J. A. K.; Puschmann, H. OLEX2: A complete structure solution, refinement and analysis program. *J. Appl. Crystallogr.* **2009**, *42*, 339−341.
(53) Petříček, V.; Dušek, M.; Palatinus, L. Crystallographic computing system JANA2006: general features. *Z. Kristallogr. - Cryst. Mater.* **2014**, *229*, 345−352.
(54) Hohenberg, P.; Kohn, W. Inhomogeneous Electron Gas. *Phys. Rev.* **1964**, *136*, B864−B871.
(55) Perdew, J. P.; Burke, K.; Ernzerhof, M. Generalized Gradient Approximation Made Simple. *Phys. Rev. Lett.* **1996**, *77*, 3865−3868.
(56) Clark, S. J.; Segall, M. D.; Pickard, C. J.; Hasnip, P. J.; Probert, M. I. J.; Refson, K.; Payne, M. C. First principles methods using CASTEP. *Z. Kristallogr.* **2005**, *220*, 567−570.
(57) Lejaeghere, K.; Bihlmayer, G.; Björkman, T.; Blaha, P.; Blügel, S.; Blum, V.; Caliste, D.; Castelli, I. E.; Clark, S. J.; Dal Corso, A.; et al. Reproducibility in density functional theory calculations of solids. *Science* **2016**, *351* (6280), aad3000.
(58) Monkhorst, H. J.; Pack, J. D. Special points for Brillouin-zone integrations. *Phys. Rev. B* **1976**, *13*, 5188−5192.
(59) Milman, V.; Warren, M. C. Elasticity of hexagonal BeO. *J. Phys.: Condens. Matter* **2001**, *13*, 241−251.
(60) Baroni, S.; de Gironcoli, S.; Dal Corso, A.; Giannozzi, P. Phonons and related crystal properties from density-functional perturbation theory. *Rev. Mod. Phys.* **2001**, *73*, 515−562.
(61) Refson, K.; Tulip, P. R.; Clark, S. J. Variational density-functional perturbation theory for dielectrics and lattice dynamics. *Phys. Rev. B* **2006**, *73*, 155114−1.
(62) Miwa, K. Prediction of Raman spectra with ultrasoft pseudopotentials. *Phys. Rev. B* **2011**, *84*, 094304−1.
(63) Dubrovinsky, L. S.; Dubrovinskaia, N. A.; Swamy, V.; Muscat, J.; Harrison, N. M.; Ahuja, R.; Holm, B.; Johansson, B. The hardest known oxide. *Nature* **2001**, *410*, 653−654.
(64) Dubrovinskaia, N.; Dubrovinsky, L. High-pressure silica polymorphs as hardest known oxides. *Mater. Chem. Phys.* **2001**, *68*, 77−79.
(65) Stangarone, C.; Angel, R. J.; Prencipe, M.; Mihailova, B.; Alvaro, M. New insights into the zircon-reidite phase transition. *Am. Mineral.* **2019**, *104*, 830−837.
(66) Mihailova, B.; Waeselmann, N.; Stangarone, C.; Angel, R. J.; Prencipe, M.; Alvaro, M. The pressure-induced phase transition (s) of $ZrSiO_4$: revised: Experimental proof for the existence of a new high-pressure polymorph of zircon. *Phys. Chem. Miner.* **2019**, *46*, 807−814.

https://doi.org/10.1021/acs.inorgchem.5c03033
Inorg. Chem. 2025, 64, 21893−21902

(67) Murnaghan, F. Finite Elastic Strain of Cubic Crystals. *Proc. Natl. Acad. Sci. U. S. A.* **1944**, *30*, 244−247.
(68) Birch, F. Finite Elastic Strain of Cubic Crystals. *Phys. Rev.* **1947**, *71*, 809.
(69) Angel, R. J.; Alvaro, M.; Gonzalez-Platas, J. EosFit7c and a Fortran module (library) for equation of state calculations. *Z. Kristallogr. - Cryst. Mater.* **2014**, *229*, 405−419.
(70) Zhang, J.; Reeder, R. J. Comparative compressibilities of calcite-structure carbonates: Deviations from empirical relations. *Am. Mineral.* **1999**, *84*, 861−870.
(71) Liang, W.; Yin, Y.; Li, Z.; Li, R.; Li, L.; He, Y.; Dong, H.; Li, Z.; Yan, S.; Zhai, S.; et al. Single crystal growth, crystalline structure investigation and high-pressure behavior of impurity-free siderite ($FeCO_3$). *Phys. Chem. Miner.* **2018**, *45*, 831−842.
(72) Hazen, R. M.; Finger, L. W. Crystal structure and compressibility of zircon at high pressure. *Am. Mineral.* **1979**, *64*, 196−201.
(73) Biedermann, N.; Winkler, B.; Speziale, S.; Reichmann, H.-J.; Koch-Müller, M. Single-crystal elasticity of $SrCO_3$ by Brillouin spectroscopy. *High Pressure Res.* **2017**, *37*, 181−192.
(74) Spahr, D.; Bayarjargal, L.; Bykova, E.; Bykov, M.; Brüning, L.; Kovalev, V.; Milman, V.; Wright, J.; Winkler, B. 6-Fold-Coordinated Beryllium in Calcite-Type $Be[CO_3]$. *Inorg. Chem.* **2024**, *63*, 19513−19517.
(75) Milman, V.; Akhmatskaya, E.; Nobes, R.; Winkler, B.; Pickard, C.; White, J. Systematic ab initio study of the compressibility of silicate garnets. *Acta Crystallogr., Sect. B: struct. Sci.* **2001**, *57*, 163−177.
(76) Hazen, R. M.; Downs, R. T.; Jones, A. P.; Kah, L. Carbon mineralogy and crystal chemistry. *Rev. Mineral Geochem.* **2013**, *75*, 7−46.

https://doi.org/10.1021/acs.inorgchem.5c03033
Inorg. Chem. 2025, 64, 21893−21902